Advanced Startup and Smooth Transition to Sensorless Field Oriented Control for CSI-Fed PMSM Drives in Submersible Pumps

Milad Bahrami-Fard, *Graduate Student Member, IEEE*, Majid Ghasemi Korrani, *Member, IEEE*, Mohammad Rastegar, *Student Member, IEEE*, and Babak Fahimi, *Fellow, IEEE*

***Abstract*—This article introduces a reliable startup method with a smooth transition to sensorless field-oriented control (FOC) in current source inverter (CSI) fed permanent magnet synchronous motor drives used in submersible pump applications. The strategy ensures a smooth transition to sensorless control, enhancing efficiency, and improves the reliability of the drive system. The proposed method minimizes speed and current oscillations during the transition stages. Furthermore, the proposed method addresses these issues by eliminating the error between the estimated and reference frames. Subsequently, using the proposed error compensation strategy, the error between the real and estimated frames is corrected. This method ensures a smooth transition from synchronous startup to sensorless FOC without requiring exact *q*-axis current or alignment error calculations while minimizing speed and current oscillations. It offers a robust, adaptive shift from I-f startup to FOC under varying conditions. Additionally, the proposed position error compensation corrects rotor discrepancies from dead-time, control delays, and parameter variations, improving torque and flux control, reducing *d*-axis current and torque ripple, lowering copper losses, and eliminating steady-state errors. This results in a faster, more reliable transition, avoiding prolonged startup durations and enhancing system stability. Simulation and experimental results validate the method's effectiveness, demonstrating minimal oscillations in speed and current.**

***Index Terms*—Current source inverter (CSI), long cable, permanent magnet synchronous motor (PMSM) drives, sensorless control, submersible pumps.**

I. Introduction

PERMANENT magnet synchronous motor (PMSM) drive systems have long been popular due to their high efficiency, excellent dynamic properties, and high power density. Field-oriented control (FOC) is the most common method for precise control of torque and speed in this family of motors [1], [2], [3], [4], [5], [6]. High-performance control strategies often use sensors for accurate rotor position and speed, but these sensors increase costs and reduce reliability in harsh environments such as those seen in submersible pumps that are used in oil and gas industry. In fact, for submersible pump applications that operate 3–4 km under the surface of earth elimination of position sensors are mandatory [7]. The position sensorless techniques are classified into high-frequency injection methods [8], [9], [10], [11], [12] (used for zero- and low-speed operation but prone to noise), and model-based methods [13], [14], [15], [16], [17] (suitable for medium- and high-speed operations). Signal injection methods function based on detection of rotor magnetic saliency, while model-based methods typically use an observer for back EMF measurement and a phase-locked loop (PLL) to track motor velocity and rotor position. To achieve sensorless FOC across the entire speed range for PMSMs, combining two methods is necessary, however this increases the complexity of the controller and compromises its reliability [18]. Moreover, most signal injection techniques require highly accurate filters, making them difficult to implement. Moreover, because signal injection depends on rotor saliency, it becomes particularly challenging to apply it to surface-mounted PMSMs, which inherently lack saliency. For numerous industrial applications, such as fans and pumps, where high dynamic performance at low speeds is not essential, signal injection method may not be needed since the primary objective is simply to start the motor. In such cases, a more straightforward approach like synchronous I-f control is more appropriate.

The current source inverter (CSI) offers many advantages, including four-quadrant operation, inherent short circuit protection, voltage boost capacity, and motor-friendly waveforms with low *dv/dt* [19], [20], [21]. It is widely used in medium-voltage, high-power electric drive applications, such as petrochemical, mining, and metal processing industries, as well as in pumping. In applications that require long cables like submersible pumps, CSI-fed drive configurations outperform voltage source inverters (VSIs) [22]. While most sensorless drive studies have focused on VSI-fed drives, research on sensorless CSI-fed drives is far from exhausted.

The back-EMF-based method is most effective at medium to high speeds, requiring a startup procedure and a robust back EMF estimator to accelerate the motor to a speed where back EMF is accurately sensed. The V-f method is a simple, open-loop startup strategy for induction motors but can be unstable under load due to the lack of current feedback [23]. In contrast, the

Received 22 March 2025; accepted 3 May 2025. Date of publication 6 May 2025; date of current version 30 June 2025. Recommended for publication by Associate Editor T. Shi. *(Corresponding author: Milad Bahrami-Fard.)*

The authors are with the Department of Electrical and Computer Engineering, University of Texas at Dallas, Richardson, TX 75080 USA (e-mail: mxb210105@utdallas.edu).

Color versions of one or more figures in this article are available at https://doi.org/10.1109/TPEL.2025.3567425.

Digital Object Identifier 10.1109/TPEL.2025.3567425

I-f method, applied to PMSMs in [24], uses closed-loop current regulation without position feedback, employing a ramp speed command to determine rotor position. This ensures smooth acceleration with minimal torque ripple and provides a more stable startup than the V-f method [25]. It is important to note that the I-f method always exhibits a deviation between the used synchronous frame of reference and actual rotor's frame of reference, which increases with the magnitude of current [25]. For pump applications, the reference current is often set high during startup to handle heavy loads. Although the I-f method and back EMF estimators are simple and robust, the key challenge is the transition between I-f synchronous starting and sensorless FOC. Therefore, designing an effective transition period is crucial for a smooth switch to sensorless FOC. Various nonideal factors, such as saturation-related deviations in stator self-inductance (i.e., L_s), computation time, feedback-related control delays, and pulsewidth modulation (PWM) of the inverter, can increase the deviation between the estimated and the actual rotor positions, making the transition more difficult and impacting torque and speed stability [26], [27], [28], [29], [30], [31].

In [24], a first-order compensator aligns the synchronous rotating reference frame with the rotor position from the back-EMF-based sensorless method, but its effectiveness depends heavily on compensator parameters [32], [33], making it difficult to adapt across different drive conditions. Additionally, it struggles to synchronize with FOC controllers during the transition, causing oscillations. In [32], the transition is managed by gradually decreasing the deviating angle based on the reference current, but this method prolongs startup and introduces torque ripples at high speeds, making it sensitive to errors. Both approaches in [24] and [32] assume negligible rotor position errors, but real-world factors, such as inverter dead-time, parameter variations, and filtering effects cause estimation discrepancies, leading to speed and current fluctuations. In contrast, the proposed method is robust to parameter variations, eliminates position errors through rotor error compensation, maintains closed-loop position estimation during transition, and enables a faster, more stable shift to FOC, reducing startup time, torque ripple, and copper losses while improving overall system performance. Injecting a constant current achieves a stable transition via feed-forward compensation in the current loop [34], but delays I-f startup while ensuring stability. In [35], a speed-dependent weighting factor was used to rotate the synchronous reference frame, but like the first-order compensator, finding appropriate parameters for convergence was challenging, and the study lacked a detailed stability analysis and design guidelines for the I-f method.

This article introduces a new startup strategy for a smooth torque and speed transition from the synchronous startup stage to the sensorless FOC stage. For a smooth transition between the I-f starting and sensorless FOC, precise alignment of the synchronous reference frame and the actual rotor frame is crucial. Most existing approaches attempt to achieve this alignment by reducing the reference q-axis current and making the d-axis current equal to zero. However, accurately determining the minimum required q-axis current is challenging, and the d-axis current may not be exactly zero prior to the transition. The proposed method addresses these issues by first eliminating the error between the estimated and reference frames. Then, using an error compensation strategy, the error between the real and estimated frames is gradually corrected. This approach guarantees a smooth transition from startup to sensorless FOC without the need for calculating the exact minimum q-axis current or the error between the real and estimated frame alignment, while minimizing speed and current oscillations. Additionally, a position error compensation strategy has been introduced to correct rotor position discrepancies, irrespective of their sources. The contribution of this article is specified as follows.

1) A robust and adaptive transition method eliminates the need for precise tuning required in first-order compensator-based approaches [24], enabling a seamless shift from I/f startup to FOC under varying drive conditions and loads.
2) A position error compensation strategy corrects rotor position discrepancies caused by inverter dead-time, control delays, and parameter variations, ensuring accurate torque and flux control. Its ability to eliminate estimation errors regardless of their origin makes it a versatile and reliable solution for various applications.
3) Improved efficiency and stability are achieved by reducing d-axis current, minimizing torque ripple, and lowering copper losses, while eliminating steady-state errors for precise motor operation.
4) A faster and more reliable transition is enabled by estimated position feedback, avoiding the prolonged startup durations of conventional methods [32] while maintaining system stability.

The rest of this article is organized as follows. Section II explains the fundamentals of sensorless control in CSI-fed PMSM drives, including the EMF-based observer derived from the PMSM model. Section III analyzes the I-f startup process, discusses non-ideal factors causing position estimation errors, and presents the proposed smooth transition to sensorless control strategy. Section IV presents and discusses the simulation results of the proposed strategy. Section V provides experimental validation. Finally, Section VI concludes the article.

II. Sensorless Control of the CSI-Fed PMSM

Fig. 1 depicts the CSI-fed PMSM drive system with a long cable connection, comprising a passive rectifier, an asymmetric H-bridge, a CSI, a dc inductor, and output capacitor filters. The asymmetric H-bridge regulates the dc current to maintain a constant dc-link current. The motor speed and torque are controlled by a CSI using a FOC methodology. Mathematical model of a surface-mounted PMSM, expressed in dq-frame, is given as follows:

$$L_s\left(\frac{di_d}{dt}\right) = -R_s i_d + \omega_e L_s i_q + u_d \tag{1}$$

$$L_s\left(\frac{di_q}{dt}\right) = -R_s i_q - \omega_e L_s i_d - \omega_e \psi_f + u_q \tag{2}$$

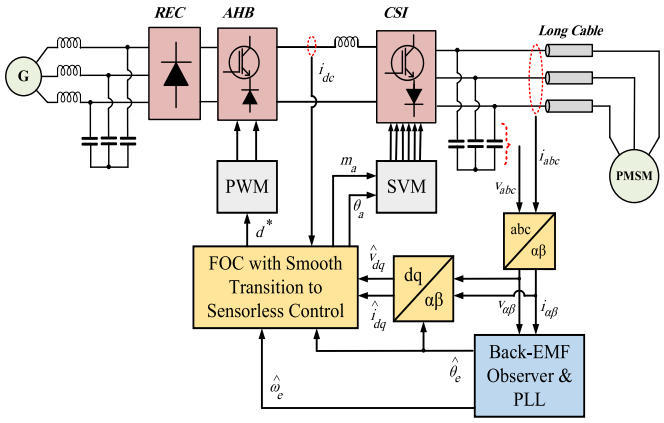

Fig. 1. CSI-fed PMSM drive system with a long cable connection for submersible pump applications.

where i_d, i_q and u_d, u_q are the stator currents and voltages, in direct and quadrature axis respectively, ω_e is the rotor electrical speed, ψ_f is the PM-originated flux linkage, R_s is the stator resistance, and L_s is the synchronous inductance.

The block diagram of the sensorless FOC for the PMSM based on back-EMF observer with the proposed smooth transition to sensorless control strategy is illustrated in Fig. 2. To estimate the rotor position in PMSMs, the mathematical model of the surface-mounted PMSM, expressed in a stationary reference frame ($\alpha\beta$), is given as

$$\begin{bmatrix} u_\alpha \\ u_\beta \end{bmatrix} = pL_s \begin{bmatrix} i_\alpha \\ i_\beta \end{bmatrix} + R_s \begin{bmatrix} i_\alpha \\ i_\beta \end{bmatrix} + \psi_f \omega_e \begin{bmatrix} -\sin(\theta_e) \\ \cos(\theta_e) \end{bmatrix} \tag{3}$$

where, u_α and u_β are the α–β-axis stator voltage components, i_α and i_β are the α–β-axis stator current components, θ_e is the rotor electrical position, and p is the differential operator, respectively. The back EMF for each phase can be described as:

$$e_\alpha = -\omega_e \psi_f \sin(\theta_e) \tag{4}$$

$$e_\beta = \omega_e \psi_f \cos(\theta_e). \tag{5}$$

The presented EMF-based observer is constructed based on the PMSM model. Utilizing the fundamentals of linear control theory, the EMF-based observer is formulated and the resulting equations are given as

$$p\dot{\boldsymbol{E}}_{\boldsymbol{\alpha\beta}} = \underbrace{\begin{bmatrix} 0 & -\omega_e \\ \omega_e & 0 \end{bmatrix}}_{\boldsymbol{A}_{11}} \dot{\boldsymbol{E}}_{\boldsymbol{\alpha\beta}} + \underbrace{\begin{bmatrix} \frac{1}{L_s} & 0 \\ 0 & \frac{1}{L_s} \end{bmatrix}}_{\boldsymbol{J}_1} \tilde{\boldsymbol{I}}_{\boldsymbol{\alpha\beta}} \tag{6}$$

$$p\dot{\boldsymbol{I}}_{\boldsymbol{\alpha\beta}} = \underbrace{\begin{bmatrix} -\frac{1}{L_s} & 0 \\ 0 & -\frac{1}{L_s} \end{bmatrix}}_{\boldsymbol{A}_{21}} \dot{\boldsymbol{E}}_{\boldsymbol{\alpha\beta}} + \underbrace{\begin{bmatrix} -\frac{R_s}{L_s} & 0 \\ 0 & -\frac{R_s}{L_s} \end{bmatrix}}_{\boldsymbol{A}_{22}} \dot{\boldsymbol{I}}_{\boldsymbol{\alpha\beta}} + \underbrace{\begin{bmatrix} \frac{1}{L_s} & 0 \\ 0 & \frac{1}{L_s} \end{bmatrix}}_{\boldsymbol{B}_1} \boldsymbol{U}^*_{\boldsymbol{\alpha\beta}} + \underbrace{\begin{bmatrix} j & 0 \\ 0 & j \end{bmatrix}}_{\boldsymbol{J}_2} \tilde{\boldsymbol{I}}_{\boldsymbol{\alpha\beta}} \tag{7}$$

where j is a positive feedback gain to make sure the observer is asymptotically stable. Additionally, $\boldsymbol{U}^*_{\boldsymbol{\alpha\beta}}$ represents the stator voltage input vector, while $\tilde{\boldsymbol{I}}_{\boldsymbol{\alpha\beta}}$ denotes the estimation error vector for the stator currents as follows:

$$\dot{\boldsymbol{I}}_{\boldsymbol{\alpha\beta}} = \begin{bmatrix} \dot{i}_\alpha \\ \dot{i}_\beta \end{bmatrix}, \dot{\boldsymbol{E}}_{\boldsymbol{\alpha\beta}} = \begin{bmatrix} \dot{e}_\alpha \\ \dot{e}_\beta \end{bmatrix}, \boldsymbol{U}^*_{\boldsymbol{\alpha\beta}} = \begin{bmatrix} e^*_\alpha \\ e^*_\beta \end{bmatrix} \tag{8}$$

$$\tilde{\boldsymbol{I}}_{\boldsymbol{\alpha\beta}} = \begin{bmatrix} \dot{i}_\alpha \\ \dot{i}_\beta \end{bmatrix} - \begin{bmatrix} i_\alpha \\ i_\beta \end{bmatrix}. \tag{9}$$

The equations of the PMSM model can subsequently be written in the standard form (10)

$$\dot{\boldsymbol{X}}_{\boldsymbol{\alpha\beta}} = \boldsymbol{A}\dot{\boldsymbol{X}}_{\boldsymbol{\alpha\beta}} + \boldsymbol{B}\boldsymbol{U}^*_{\boldsymbol{\alpha\beta}} + \boldsymbol{J}\tilde{\boldsymbol{I}}_{\boldsymbol{\alpha\beta}} \tag{10}$$

where system matrices $\dot{\boldsymbol{X}}_{\boldsymbol{\alpha\beta}}$, $\boldsymbol{A}$, $\boldsymbol{B}$, and $\boldsymbol{J}$ can be identified as follows:

$$\dot{\boldsymbol{X}}_{\boldsymbol{\alpha\beta}} = \begin{bmatrix} \dot{\boldsymbol{E}}_{\boldsymbol{\alpha\beta}} \\ \dot{\boldsymbol{I}}_{\boldsymbol{\alpha\beta}} \end{bmatrix} \tag{11}$$

$$\boldsymbol{A} = \begin{bmatrix} \boldsymbol{A}_{11} & 0 \\ \boldsymbol{A}_{21} & \boldsymbol{A}_{22} \end{bmatrix} \tag{12}$$

$$\boldsymbol{B} = \begin{bmatrix} 0 \\ \boldsymbol{B}_1 \end{bmatrix} \tag{13}$$

$$\boldsymbol{J} = \begin{bmatrix} \boldsymbol{J}_1 \\ \boldsymbol{J}_2 \end{bmatrix}. \tag{14}$$

In some cases, significant harmonic content may appear in the estimated back EMFs, as explored in [36] and [37]. Consequently, low-pass filters can be utilized before applying the estimated back EMFs into the PLL. However, in this article, a back-EMF filter was not implemented since the experimental tests did not reveal any prominent harmonics in the observer estimates.

A. Output Filter Capacitor Selection and Voltage Control

The switching nature of a CSI results in a quasi-square output waveform with significant harmonic content. Without proper filtering, these harmonics can lead to excessive voltage stress on motor windings, electromagnetic interference, and increased torque ripple, negatively impacting motor performance. The output capacitor C_f acts as a low-pass filter, attenuating high-frequency harmonics and producing a more sinusoidal voltage waveform, which improves motor efficiency and reduces acoustic noise. While the output capacitor significantly reduces voltage harmonics and motor winding stress, it also introduces resonance challenges. The capacitor interacts with the stator inductance to form a resonant circuit that can destabilize the system if not adequately controlled. This resonance issue is exacerbated at high speeds, where the fundamental frequency approaches the LC resonance frequency. Therefore, careful capacitor selection is necessary to balance harmonic filtering and resonance avoidance.

The FOC scheme for CSI-fed PMSM differs from the VSI-fed version by lacking voltage references, while also requiring consideration of the current flowing into the capacitors due to the output filter. In order to improve the harmonic performance on the motor side with CSI-fed PMSM drives, the capacitor voltage control is employed. This method enhances the system's

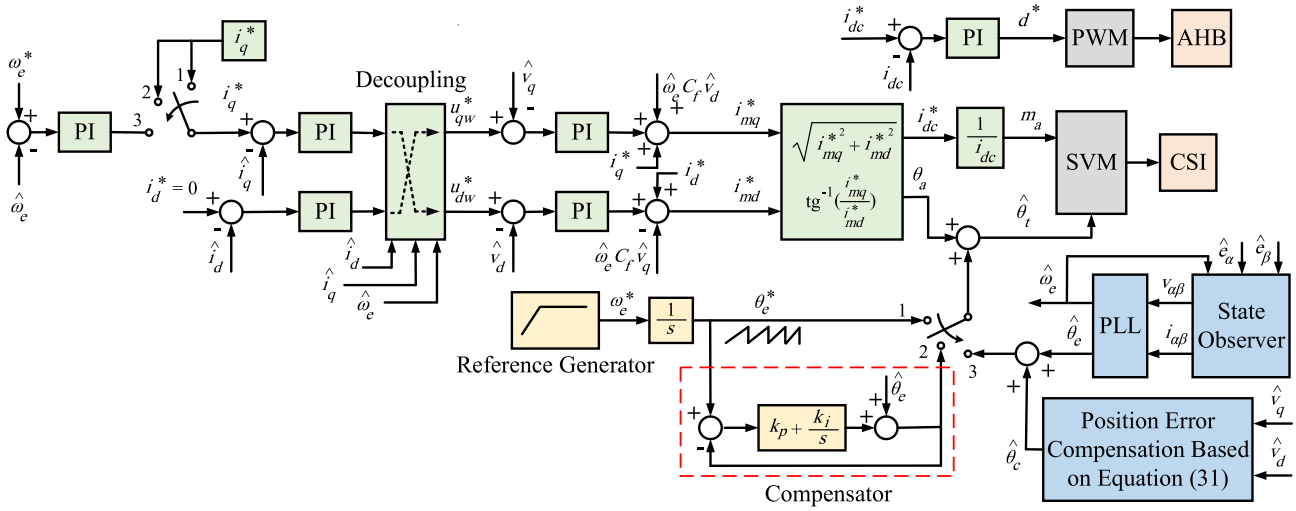

Fig. 2. FOC control of the CSI-fed PMSM drive system with proposed smooth transition strategy.

dynamic performance and stability by dynamically regulating the capacitor voltage references within the current control loop. By compensating for the capacitor currents, capacitor voltage control helps suppress resonances and improve overall system efficiency, leading to better motor operation. In this approach, the current references i_d^* and i_q^* for the CSI are modified to include the dynamic capacitor currents, represented by i_{cd}^* and i_{cq}^*, as follows:

$$i_{mq}^* = i_q^* + \hat{\omega}_e C_f \hat{v}_d + i_{cq}^* \tag{15}$$

$$i_{md}^* = i_d^* - \hat{\omega}_e C_f \hat{v}_q + i_{cd}^* \tag{16}$$

where, i_d^* and i_q^* are the dq-axis stator current references, C_f is the capacitance, and $\hat{v}_d$ and $\hat{v}_q$ are the dq-axis stator voltages. The terms i_{cd}^* and i_{cq}^* represent the compensation currents for the capacitors, which are computed using a PI controller. The capacitor voltage control is implemented by calculating the compensation currents i_{cd}^* and i_{cq}^* as

$$i_{cq}^* = K_{pv}\left(u_{qw}^* - \hat{v}_q\right) + K_{iv}\int\left(u_{qw}^* - \hat{v}_q\right) \tag{17}$$

$$i_{cd}^* = K_{pv}\left(u_{dw}^* - \hat{v}_d\right) + K_{iv}\int\left(u_{dw}^* - \hat{v}_d\right) \tag{18}$$

where u_{dw}^* and u_{qw}^* are the reference values for the capacitor voltages, and $\hat{v}_d$ and $\hat{v}_q$ are the actual capacitor voltages. The gains K_{pv} and K_{iv} are the proportional and integral gains for the capacitor voltage control loop. Finally, the capacitor voltage references are regulated through the stator current control loops, which are also governed by proportional-integral controllers (PI controllers). The reference voltages are given by

$$u_{qw}^* = K_{pi}\left(i_q^* - \hat{i}_q\right) + K_{ii}\int\left(i_q^* - \hat{i}_q\right) \tag{19}$$

$$u_{dw}^* = K_{pi}\left(i_d^* - \hat{i}_d\right) + K_{ii}\int\left(i_d^* - \hat{i}_d\right) \tag{20}$$

where K_{pi} and K_{ii} are the proportional and integral gains for the stator current control loop. These PI controllers ensure that the stator current references are correctly tracked and that the capacitor voltage follows the desired low-bandwidth reference, thereby improving the dynamic performance of the system and effectively suppressing LC resonance. By incorporating the capacitor voltage control loop into the control scheme, the overall system stability and bandwidth are significantly improved, leading to better dynamic response and reduced resonance caused by the output filter. The current reference and the modulation index which are related to the inverter-side current, which can be expressed as follows:

$$m_a = \frac{i_{\mathrm{dc}}^*}{i_{\mathrm{dc}}} = \sqrt{\left(i_{mq}^*\right)^2 + \left(i_{md}^*\right)^2}/i_{\mathrm{dc}}. \tag{21}$$

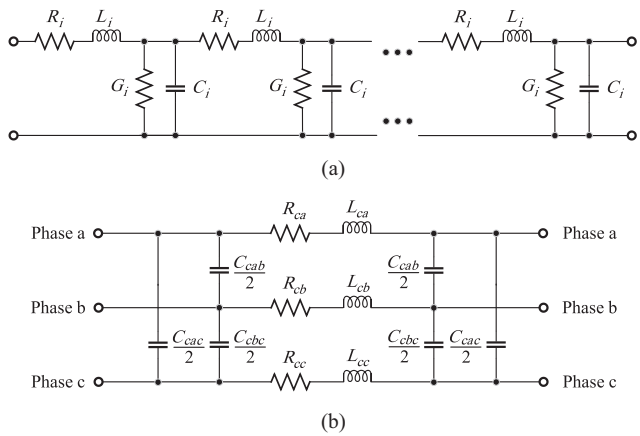

Fig. 3. Modeling of long motor cable: (a) Lossy distributed transmission line model. (b) π equivalent model of the long cable.

B. Transmission Line Model

In inverter-fed motor drive systems, long cables introduce significant electrical effects that must be carefully modeled and ed. As illustrated in Fig. 3(a), these cables can be represented as transmission lines with distributed resistance (R_i), inductance (L_i), capacitance (C_i), and conductance (G_i) per unit length. For simplified analysis, a transmission line approximation is

often used, assuming $G_i = \infty$, as shown in Fig. 3(b). However, in practical applications, accurately modeling the electrical characteristics of long cables is essential for understanding their impact on system performance. A more precise representation is achieved using a π-model, which accounts for the distributed R, L, and C parameters. This model is critical for evaluating key effects such as voltage reflections that may cause overvoltage at motor terminals, harmonic resonance that affects waveform quality and increases losses, and signal attenuation that can degrade sensorless position estimation. To validate the impact of long cables in a practical setting, a π-model with lumped parameters ($R_c = 11.76\ \Omega$, $L_c = 9.7\,\text{mH}$, $C_c = 111\,\text{nF}$) is incorporated between the CSI and PMSM. To assess the system's robustness against long-distance transmission effects, the proposed method is evaluated in real-world industrial motor drive applications, where extended cabling is a common challenge.

III. Startup Strategy for Sensorless Control of the CSI-Fed PMSM Drives

In low-speed range, the back-EMF method is hindered by the low magnitude of the back-EMF signal. Therefore, a different approach is required to accelerate the motor from standstill to a speed where the back-EMF is sufficiently large for accurate measurement. Position estimation is only accurate when the motor speed reaches at least 10% of the rated velocity [23], [24], [25]. At low speeds, the observation values $\dot{\boldsymbol{E}}_{\boldsymbol{\alpha\beta}}$ and $\tilde{\boldsymbol{I}}_{\boldsymbol{\alpha\beta}}$ are minimal, making the estimated position more prone to small interferences. This can cause the motor to lose synchronization during the startup process, specifically in the low-speed range. Consequently, an improved startup method is needed to address this issue for industrial applications.

A. I-f Startup Analysis

During the speed ramp-up, the startup procedure uses a closed current loop and an open speed loop in the synchronous reference d^*q^*-frame, as shown in Fig. 2. In this process, the reference q^*-axis current (i_q^*) is maintained constant, and the i_d^* is set to zero. The reference θ_e^* is obtained by integrating the ramp speed command (ω_e^*) as follows:

$$\theta_e^* = \int \omega_e^* dt \tag{22}$$

$$\omega_e^* = K_\omega t \tag{23}$$

where K_ω is a constant. At the start of the procedure, the d^*q^*-frame is set to a $\delta_e^* = 90^\circ$ phase lag relative to the real rotor dq-frame so that the dq-frame can start moving smoothly, ensuring no initial torque generation ($\cos 90^\circ = 0$), as shown in Fig. 4. The d^*q^*-frame rotates as the ramp speed command is integrated. As angle δ_e^* decreases, the q-axis current (i_q) increases proportional to $i_q^* \cos\delta_e^*$. Once i_q generates sufficient torque to exceed the load torque, the rotor begins to rotate, and δ_e^* converges to a fixed value depending on the load and acceleration. The relationship between the d^*q^*-axis currents and the actual currents is defined as follows:

$$i_q = i_q^* \cos\delta_e^* - i_d^* \sin\delta_e^* \tag{24}$$

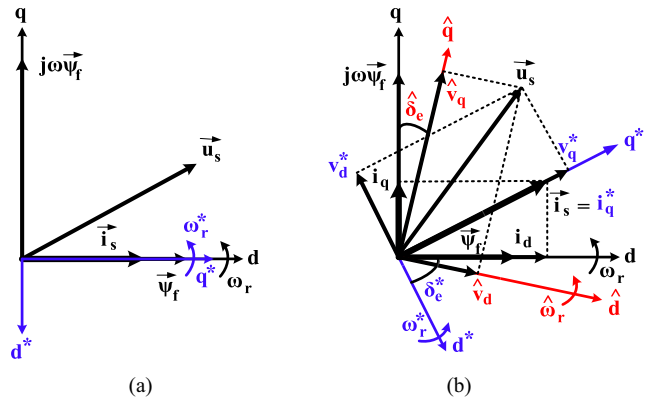

Fig. 4. Diagram of the virtual synchronous d^*q^*-reference frame, real rotor dq frame, and estimated $\hat{d}\hat{q}$ frame. (a) Initial startup. (b) Acceleration.

$$i_d = i_q^* \sin\delta_e^* + i_d^* \cos\delta_e^*. \tag{25}$$

If angle δ_e^* becomes negative, the motor's self-stabilization is lost, leading to a rapid decrease in speed and potentially stall of the rotor. To prevent this, it is crucial to keep the d^*q^*-axis lagging behind the rotor dq-axis with sufficient margin in angle δ_e^*. This is typically achieved by maintaining a high enough q^*-axis current. However, when i_q^* is greater than i_q, it creates an angle error (δ_e^*) between the synchronous reference frame and the real rotor frame. Although the startup can technically occur with any initial phase difference between the synchronous reference d^*q^*-frame and the actual rotor dq frame, the specific angle and operating region significantly impact the system's stability. Depending on the initial phase angle, oscillations may occur in the motor's position and speed, leading to an unstable or inefficient startup. To further analyze this, simulations were conducted for different initial phase angles ($\delta_e^* = 0$, $\delta_e^* = 45^\circ$, and $\delta_e^* = 90^\circ$). The results, presented in Fig. 5, clearly demonstrate that initiating the startup with a 90° phase lag provides the smoothest transition, minimizing oscillations and ensuring stable motor acceleration from standstill. Therefore, an immediate switching of the speed controller from open-loop startup to closed-loop FOC control mode can cause large torque and current pulses.

Notably, this I–f starting method possesses a self-stabilizing property and inherently achieves dynamic balance when both the first and second derivatives of the angle δ_e^* are minimized. The connection between the synchronous frame q^*-axis current i_q^* and the actual motor torque T_e can be defined as follows:

$$T_e = 1.5Pi_q^* \cos\delta_e^* \left(\psi_f + (L_d - L_q)\, i_q^* \sin\delta_e^*\right) = \approx 1.5Pi_q^* \cos\delta_e^* \psi_f \tag{26}$$

where P is the number of pole pairs and ψ_f is the PM flux linkage. The term $(L_d - L_q)i_q^* \sin\delta_e^*$ in (19) is negligible when compared to the permanent magnet flux linkage ψ_f. Therefore, the state equation for the startup procedure can be formulated as follows:

$$\frac{d\theta_e}{dt} = \omega_r - \omega_e^* \tag{27}$$

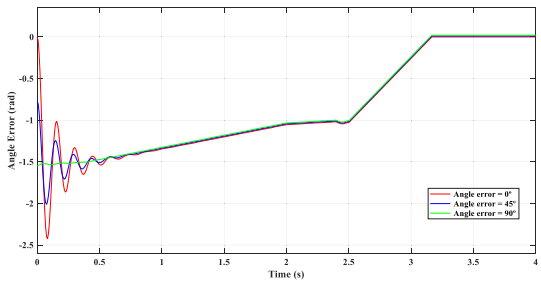

(a)

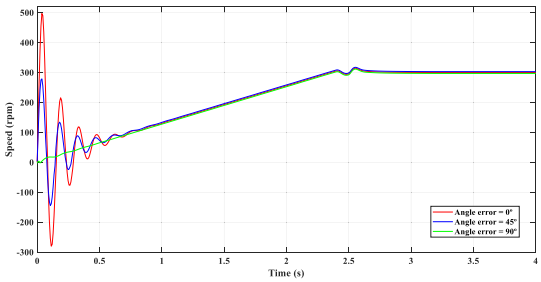

(b)

Fig. 5. Angle error and speed response for different initial phase angles. (a) Angle error between virtual synchronous d^*q^*-reference frame and actual rotor dq frame. (b) Speed response for different initial angle errors ($\delta_e^* = 0$, $\delta_e^* = 45°$, and $\delta_e^* = 90°$).

$$\frac{d^2\theta_e}{dt^2} = \frac{1.5Pi_q^* \cos\delta_e^*\psi_f - T_L}{J} - K_\omega \tag{28}$$

where J is the inertia of the motor and T_L is the load torque. The second derivative of the angle δ_e^* is key to ensuring that the virtual synchronous reference frame does not deviate too much during the transition. This term represents the torque dynamics and compensates for any imbalance between the load torque and the motor's inertial response. The dynamic balance of the system is achieved only when both the first and second derivatives of θ_e are either maintained at zero or fluctuate around zero. As a result, the limiting value of K_ω is determined in (29), since the second derivative of θ_e cannot remain constantly positive under any load conditions. To ensure stability and avoid significant deviations from the real rotor frame, the second derivative of δ_e^* should remain small or oscillate within a tight range. The maximum allowable value for K_ω can be derived by setting the second derivative of δ_e^* to zero, which leads to the following condition for stability

$$K_\omega < \frac{1.5Pi_q^* \cos\delta_e^*\psi_f - T_{L,\max}}{J} \tag{29}$$

where, $T_{L,\max}$ represents the maximum load torque during startup. A lower value of K_ω will prolong the startup process but helps to minimize speed fluctuations during this phase. Furthermore, the angle δ_e^* is constrained to an effective range during the motor startup to ensure smooth acceleration without significant torque oscillations. The relationship between the load torque and the deviation δ_e^* dictates the motor's torque response. As the load torque increases, the acceleration decreases, and δ_e^* becomes smaller, indicating a more stable startup. In addition to the constraint on K_ω, there is also a limitation on δ_e^* to ensure the dynamic balance of PMSMs. First, for proper load torque balance, $\cos\delta_e^*$ must be positive. Additionally, $\cos\delta_e^*$ should be positively correlated with the load torque to ensure that the motor torque responds appropriately to changes in load. Specifically, for a constant load, there are two balance points. However, as the load torque increases, the motor's acceleration will decrease, causing δ_e^* to reduce. In this case, when $0 < \delta_e^* < \pi/2$, $\cos\delta_e^*$ will increase as δ_e^* decreases, which leads to an increase in the motor torque and establishes a new balance. A similar process occurs when the load torque decreases.

The estimated rotor axis is denoted by the $\hat{d}\hat{q}$-axis, and Fig. 4(b) illustrates its relationship to the dq-axis. The estimated position is shown by $\hat{\theta}_e$, and the actual position is denoted by θ_e. As previously discussed, performance of FOC is directly influenced by the precision of rotor position estimation. There are multiple non-ideal elements that contribute to position estimation error. These include, saturation-related deviations in L_s, computation time, feedback-related control delays in the motor drive system, and PWM of the inverter, all of which lead to errors proportionate to rotor speed. It is difficult to quantify these inaccuracies, especially those caused by control delay (T_d). The impact of iron loss is also highly significant at high speeds, however its quantification is challenging since it depends on multiple nonideal criterions. Furthermore, because of the substantial deadtime ratio in a single switching period at high speeds, the inverter's insertion of deadtime needs a greater command voltage than the actual voltage, leading to severe position estimate inaccuracies.

Defining the difference between the estimated and the real positions as position error ($\hat{\delta}_e = \theta_e - \hat{\theta}_e$), the (1) and (2) can be transformed into the following expressions in $\hat{d}\hat{q}$-axis under steady-state condition:

$$\hat{u}_q = \omega_e L_s \hat{i}_d + \omega_e \psi_f \cos\left(\hat{\delta}_e\right) \tag{30}$$

$$\hat{u}_d = -\omega_e L_s \hat{i}_q + \omega_e \psi_f \sin\left(\hat{\delta}_e\right). \tag{31}$$

The difficulty in accurately measuring the entire estimation error caused by many non-ideal elements makes it difficult to directly compensate for $\hat{\delta}_e$. Therefore, it is necessary to investigate a method that can compensate position errors δ_e^* and $\hat{\delta}_e$ before transitioning from open-loop startup to closed-loop FOC control mode.

B. Proposed Smooth Transition to Senesorless Control Strategy

As stated previously, in the I-f startup method, the rotor position reference is initially estimated by integrating the ramp speed command. During this startup process, the reference d-axis current is set to zero, while the reference q-axis current is kept constant, and the rotor speed increases. The virtual synchronous frame, based on the reference rotor position, is used to analyze the dynamic characteristics and ensure smooth acceleration while minimizing the angle deviation between the real rotating frame and the virtual frame, which is represented

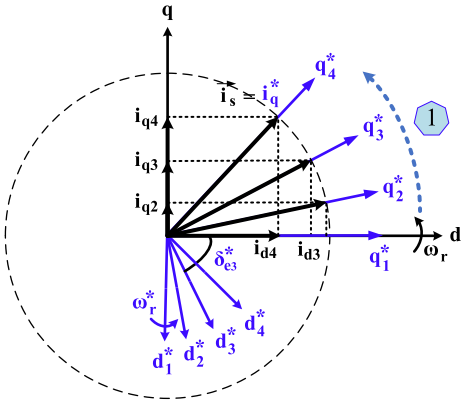

Fig. 6. Diagram of the virtual synchronous d^*q^*-reference frame and real rotor dq frame during stage 1.

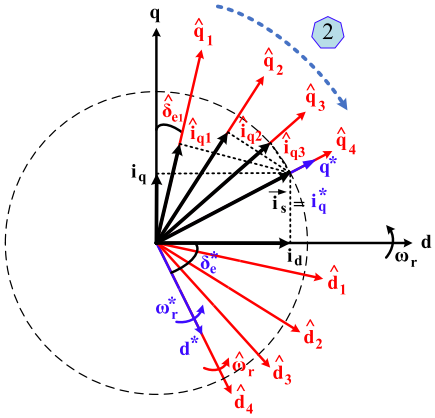

Fig. 7. Diagram of the virtual synchronous d^*q^*-reference frame, real rotor dq frame, and estimated $\hat{d}\hat{q}$ frame during stage 2.

as δ_e^*

$$\begin{bmatrix} i_q^* \\ i_d^* \end{bmatrix} = \begin{bmatrix} \cos\delta_e^* & \sin\delta_e^* \\ -\sin\delta_e^* & \cos\delta_e^* \end{bmatrix} \begin{bmatrix} i_q \\ i_d \end{bmatrix} \tag{32}$$

where i_q^*, i_d^* are the stator current components in the d^*q^* reference frame, and δ_e^* represents the angle deviation between the real rotor frame and the virtual synchronous frame. To relate the rotor flux linkage ψ_f with the stator currents i_q^*, i_d^*, the voltage equations in the d^*q^* axes of the virtual synchronous reference frame are given by

$$L_s\left(\frac{di_d^*}{dt}\right) = -R_s i_d^* + \omega_e L_s i_q^* + u_d^* \tag{33}$$

$$L_s\left(\frac{di_q^*}{dt}\right) = -R_s i_q^* - \omega_e L_s i_d^* - \omega_e \psi_f + u_q^*. \tag{34}$$

These equations describe the dynamics of the system in the virtual synchronous frame and are crucial for aligning the estimated frame with the reference frame during the startup phase before switching to the sensorless FOC. Fig. 2 depicts the block diagram of the sensorless FOC system for a CSI-fed PMSM with the proposed smooth transition strategy. The proposed sensorless control is segmented into three sequential procedures. Figs. 6, 7, and 8 show the virtual synchronous d^*q^*-reference frame, real rotor dq frame, and estimated $\hat{d}\hat{q}$ frame during

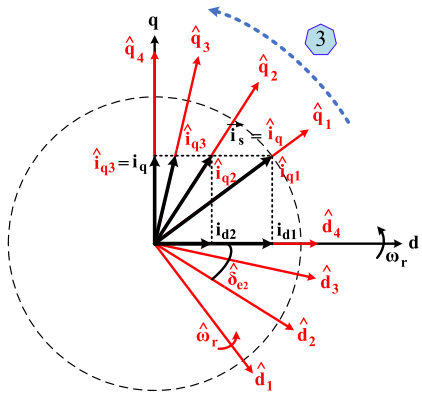

Fig. 8. Diagram of the real rotor dq frame and estimated $\hat{d}\hat{q}$ frame during stage 3.

different stages of the proposed startup and smooth transition to sensorless control.

First, the I-f method is utilized to start the motor from a standstill with low acceleration, achieving a stable desired speed where the back EMF is sufficiently high to determine the estimated position using the PLL and observer, with both switches connected to terminal 1. During the speed ramp-up, the q^*-axis current remains constant, and the d^*-axis current is set to zero. Initially, dc currents align the rotor to zero position. As shown in Fig. 6, the synchronous reference frame d^*q^* is then set to lag the actual rotor dq frame by 90 electrical degrees, causing no torque generation. As d^*q^* starts to rotate, the real q-axis current (i_q) increases with the decreasing angle δ_e^*. If i_q^* exceeds i_q, an angle error (δ_e^*) forms between the reference and rotor frames. Once the real q-axis current produces enough torque to surpass the load torque, the rotor begins to rotate, aligning the rotor dq-axes with the synchronous d^*q^*-axes.

Secondly, the compensator detailed in Fig. 2 will reduce the error between the estimated position and the reference position to zero, preparing the system for switching to terminal 2. The process is shown in Fig. 7. During this process, only the position is switched while the reference i_q^* remains constant. Since the estimated $\hat{d}\hat{q}$-frame is aligned with the virtual synchronous d^*q^*-reference frame, no significant speed or current fluctuations will occur due to the terminal switching from 1 to 2.

Finally, the switches are shifted to terminal 3, where the PLL output initially exhibits the same error calculated in the compensator, but this position error will be eliminated using the proposed error compensation strategy based on (30) and (31). The process is shown in Fig. 8. The algorithm for the proposed position error compensation is depicted in the flowchart given in Fig. 9. Switching from terminal 2 to 3 will not cause any speed or current fluctuations, as the initial output of the speed PI controller and the compensated position added to the estimated position remain consistent with the previous stage, with the error between the real and estimated positions gradually being eliminated after the terminal is shifted.

Based on (31), to completely correct the position error after shifting to terminal 3, $u_q^{'}$ must be at its maximum value (i.e., $\cos(\hat{\delta}_e) = 1$). The estimated position is adjusted using the

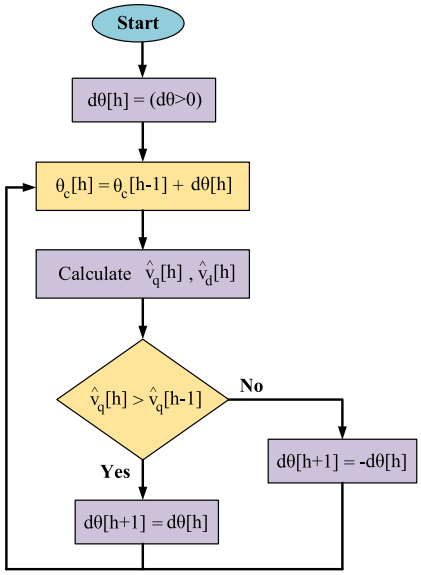

Fig. 9. Flowchart of the algorithm for the proposed position error compensation strategy.

proposed method to maintain $u_q^{'}$ at its maximum and to make sure the position error is compensated for. 'θ_c' is designated as a compensation factor utilized to rectify the position error estimation unit. The algorithm starts by initializing θ_c and assuming a variable step size '$d\theta$'. By setting "h" as the number of control cycles amplitudes of $u_q^{'}$ and $u_d^{'}$ are calculated. If $u_q^{'}$ increases, $d\theta[h]$ remains constant. Otherwise, the sign of $d\theta[h]$ is altered (i.e.,$-d\theta$) and the magnitude of the voltages are recalculated. This method will guarantee the position error will be compensated in a relatively short time without requiring complex models.

The focus on CSI control in this article is primarily due to its unique advantages in long-distance transmission systems and high-performance motor control. Unlike VSI systems, which control voltage directly, CSI systems regulate output current, offering more precise and stable control, especially in applications involving long cable runs where impedance mismatches can significantly affect performance. The CSI's ability to manage current directly is critical in scenarios such as submersible pump applications, where large torque demands and long transmission lines are common. In contrast, VSI systems typically employ inductive filters or passive dv/dt filters at the output, and do not encounter the same resonance issues or impedance challenges that arise in CSI-based systems.

Despite these differences, the fundamental principles of the proposed startup strategy can be adapted to VSI-based systems. Both CSI and VSI share common challenges, such as rotor position estimation, startup stability, and smooth transition to sensorless control. While CSI control is based on current regulation and VSI control on voltage modulation, the core strategy developed in this article, including the smooth transition from I-f startup to sensorless FOC, is applicable to both inverter types. The research highlights how the proposed three-stage startup method addresses key challenges, such as minimizing position errors and ensuring stable motor operation, making it relevant not only for CSI systems, but also for VSI-based motor drives, especially in long-line transmission scenarios. While CSI requires additional sensors compared to VSI, it is essential to weigh this tradeoff against the significant advantages that CSI offers in specific applications. For instance, in long-distance power transmission, such as submersible pumps and offshore oilfield drilling, CSI excels in handling wave reflection, harmonic amplification, and *dv/dt* issues that are common in long cable scenarios. Unlike VSI, which struggles with voltage spikes and waveform distortions due to impedance mismatches, CSI ensures stable operation through direct current control and output capacitor filtering. In addition, while various control strategies can be employed in motor drives, including methods, such as maximum torque per ampere (MTPA), which optimizes torque production while minimizing current, the control approach chosen must align with the motor's characteristics. MTPA is particularly effective in interior, where reluctance torque can be leveraged. However, in this article, FOC is employed for the surface PMSM (SPMSM), as it is the most suitable control strategy for nonsalient motors like SPMSMs.

TABLE I
SYSTEM PARAMETERS FOR BOTH SIMULATION AND EXPERIMENTAL

Parameters	Value
Equivalent resistance R_s	2.16 Ω
Equivalent inductance L_s	4.56 mH
Cable equivalent resistance R_c	11.76 Ω
Cable equivalent inductance L_c	9.7 mH
Cable equivalent capacitance C_c	111 nF
Number of pole pairs P	6
Grid voltage V_g	480 V
Grid frequency f_g	60 Hz
DC-link inductance L_{dc}	10 mH
Output filter C_o	50 uF

IV. SIMULATION RESULTS

The performance and effectiveness of the proposed startup strategy for the CSI-fed PMSM drive have been validated through simulations. The key parameters of the CSI-fed PMSM drive are given in Table I. Fig. 10 shows the simulation results of the proposed startup strategy, demonstrating a smooth transition to sensorless FOC. The I-f method starts the motor from standstill to a stable speed of 300 r/min, where the back EMF is high enough to estimate the position using the PLL and observer. As explained previously, a PI compensator is designed to drive δ_e to zero before switching the position terminal, with K_p ensuring fast response and K_i eliminating steady-state error. The final gains, $K_p = 0.2$ and $K_i = 10$, are determined through simulations and experiments to ensure a stable transition with minimal oscillations. At $t = 2.5$ s, the compensator aligns the estimated frame with the virtual reference frame. At $t = 3$ s, the terminal switches from 1 to 2 without any speed or current

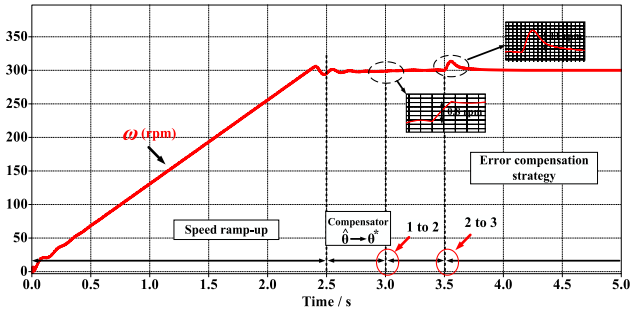

Fig. 10. Simulation waveform of the motor speed using the proposed startup strategy with a smooth transition to sensorless FOC control.

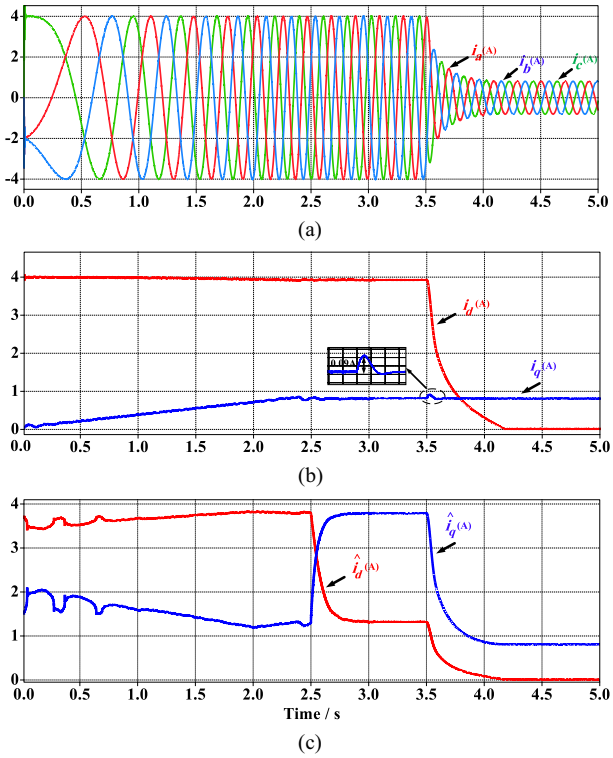

Fig. 11. Simulation results of the proposed startup strategy. (a) Three phase currents. (b) Real dq-axis currents. (c) Estimated $\hat{d}\hat{q}$-axis currents.

oscillation. Finally, at $t = 3.5$ s, the terminal switches from 2 to 3, applying the proposed compensation strategy based on (31) to align the estimated frame with the real frame. The results show minimal oscillation in speed (11 r/min), highlighting the effectiveness of the smooth transition strategy.

Fig. 11 shows the simulation waveforms of the three phases, dq-axis, and $\hat{d}\hat{q}$-axis currents during different stages using the proposed startup strategy. As can be seen from Fig. 11(b), when the terminal switches from 1 to 2, there is no oscillation in dq-axis currents. In addition, when the terminal switches from 2 to 3 and the proposed compensation strategy is applied, the dq-axis and $\hat{d}\hat{q}$-axis currents will be the same after 0.7s with minimal oscillation in current (0.09 A).

Fig. 12 shows the simulation results of the virtual synchronous, real, and estimated positions during different stages of the proposed startup. As can be seen from Fig. 12, at $t = 2.5$ s,

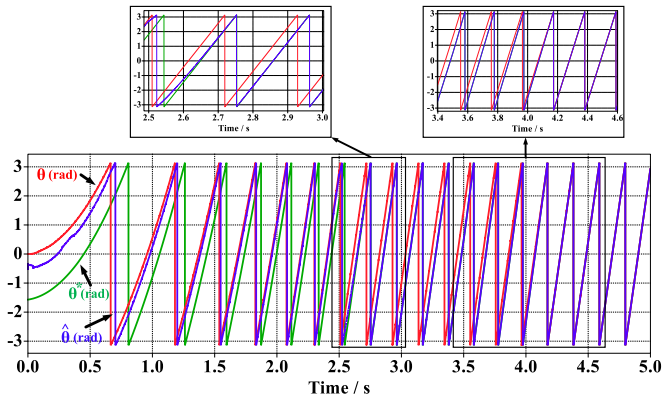

Fig. 12. Simulation results of the proposed startup strategy; virtual synchronous, real, and estimated positions.

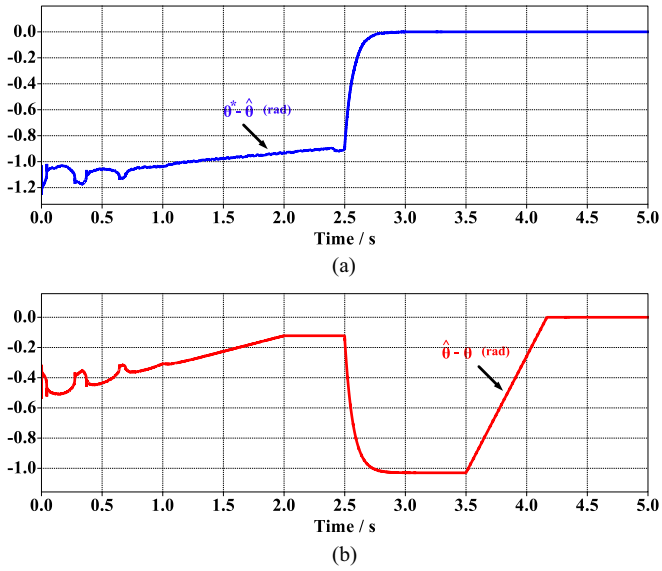

Fig. 13. Simulation results of the proposed startup strategy; (a) Angle error between estimated $\hat{d}\hat{q}$ frame and virtual synchronous d^*q^*-reference frame. (b) Angle error between actual rotor dq frame and estimated $\hat{d}\hat{q}$ frame.

the estimated frame will align with the virtual reference frame using the compensator. When the estimated frame is completely aligned with the virtual reference frame, the terminal switch from 1 to 2 at $t = 3$ s without any transients in positions, current, and speed. Finally, as is shown in Fig. 13, the error between the estimated and real positions will be eliminated using the proposed compensation strategy.

Fig. 14(a), (b) and (c), (d) illustrates the simulation outcomes of the proposed startup method under friction loads increased by factors of 3 and 4, respectively, compared to previous results. As observed, a smooth transition to FOC control is successfully achieved without any noticeable oscillations in motor speed or phase currents. This highlights the effectiveness of the proposed method, demonstrating its robustness and independence from load conditions, ensuring stable performance across all transient stages.

The explanation of steps 1 and 2 is presented separately to clearly define the components of the proposed method. By separating these steps, the role of each stage—initial startup

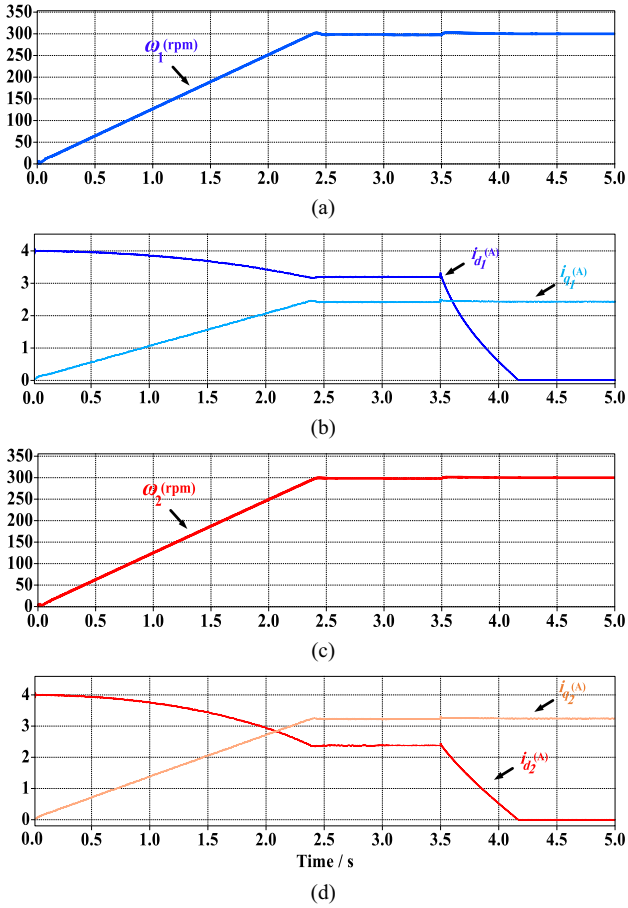

Fig. 14. Simulation results of the proposed startup strategy with different friction loads (a) Motor speed with friction load increased by a factor of 3. (b) Real dq-axis currents with friction load increased by a factor of 3. (c) Motor speed with friction load increased by a factor of 4. (d) Real dq-axis currents with friction load increased by a factor of 4.

with I-f control and alignment using the compensator—is more explicitly defined, enhancing clarity. However, these steps can be combined for a more streamlined transition. Specifically, the alignment between the reference and estimated positions can be performed during the I-f startup phase (stage 1), eliminating the need for a separate switching step between stage 1 and stage 2. This results in a direct transition to FOC at $t = 2.5$ s, improving system response while maintaining stability. Simulation results in Fig. 15 illustrate this approach, where the reference and estimated positions are aligned during startup, allowing the system to transition to sensorless FOC at $t = 2.5$ s without an additional switching step.

A. Comparison With Other Solutions

The comparison between the proposed method and conventional approaches is presented in Fig. 16(a), (b), and (c), which illustrate the speed response, angle error between the virtual synchronous reference frame and the actual rotor frame, and the real dq-axis currents. The results demonstrate that the proposed method achieves a faster and smoother transition from I/f startup to sensorless FOC compared to the methods in [24] and [32]. Specifically, the proposed method utilizes estimated position

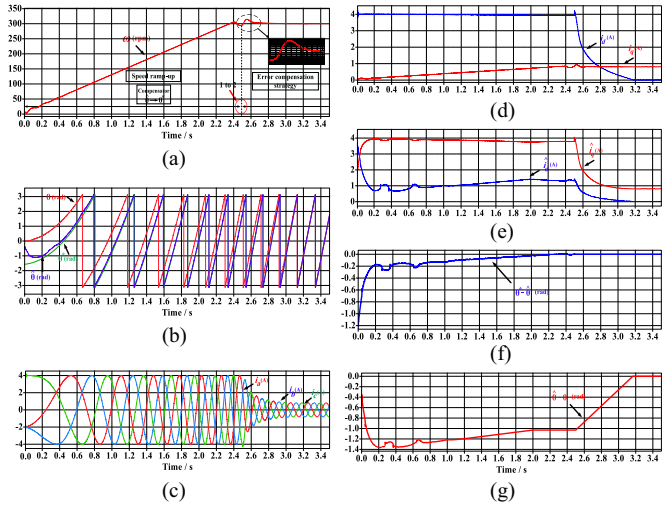

Fig. 15. Simulation results of the proposed startup strategy with a smooth transition to sensorless FOC control (a) Motor speed. (b) Virtual synchronous, real, and estimated positions (c) Three phase currents. (d) Real dq-axis currents. (e) Estimated $\hat{d}\hat{q}$-axis currents. (f) Angle error between estimated $\hat{d}\hat{q}$ frame and virtual synchronous d^*q^*-reference frame. (g) Angle error between actual rotor dq frame and estimated $\hat{d}\hat{q}$ frame.

feedback during dq-adjustment, allowing for a quicker and more stable handover, without the need for extensive tuning or prolonged startup durations. In contrast, the conventional methods rely on gradual q-axis current reduction, resulting in longer startup times and instability, particularly at high speeds. These figures clearly show the superior dynamic performance and efficiency of the proposed method, including minimal torque ripple and smoother transitions.

A detailed comparison of the proposed method and existing approaches is given in Table II. The proposed method exhibits improved robustness by eliminating sensitivity to control parameters, making it easier to tune and adaptable to varying drive conditions. Unlike the method in [32], which requires a minimum position error to avoid instability, the proposed method actively compensates for rotor position errors, ensuring a consistent and reliable transition from I/f startup to FOC. Furthermore, the proposed approach reduces d-axis current and copper losses, leading to improved efficiency and a faster, more reliable transition. Although the computational complexity is slightly higher due to the active rotor error compensation, the proposed method outperforms existing methods in terms of stability, transition speed, and dynamic performance, making it ideal for high-performance applications requiring rapid sensorless startup.

V. Experimental Results

To further validate the proposed startup strategy experimentally, we conducted a series of tests on the CSI-fed PMSM drive system with a long cable connection (1.8 km), utilizing a TMS320F28388D processor, as illustrated in Fig. 17. The key parameters of the CSI-fed PMSM drive are given in Table I. An absolute encoder is utilized exclusively to gather the actual position for comparison.

TABLE II
COMPARING THE PROPOSED METHOD WITH OTHER SOLUTIONS

Method	Advantage	Disadvantage
Traditional Method in [24]	I. Simple structure.	I. Highly sensitive to compensator parameters. II. Difficult to tune for different drive conditions. III. Sensitive to errors between estimated and real positions.
Gradient-Based Method in [32]	I. Smooth transition from I/f startup to FOC.	I. Requires a minimum position error to avoid instability. II. Prolonged startup process. III. Sensitive to errors between estimated and real positions. IV. Potential for torque ripple at high speeds.
Proposed method	I. Smooth transition from I/f startup to FOC. II. Not sensitive to control parameters. III. Active position error compensation. IV. Reduced d-axis current & copper loss. V. Faster and more reliable transition. VI. Not sensitive to errors between estimated and real rotor positions.	I. Slightly higher computational complexity due to active rotor error compensation.

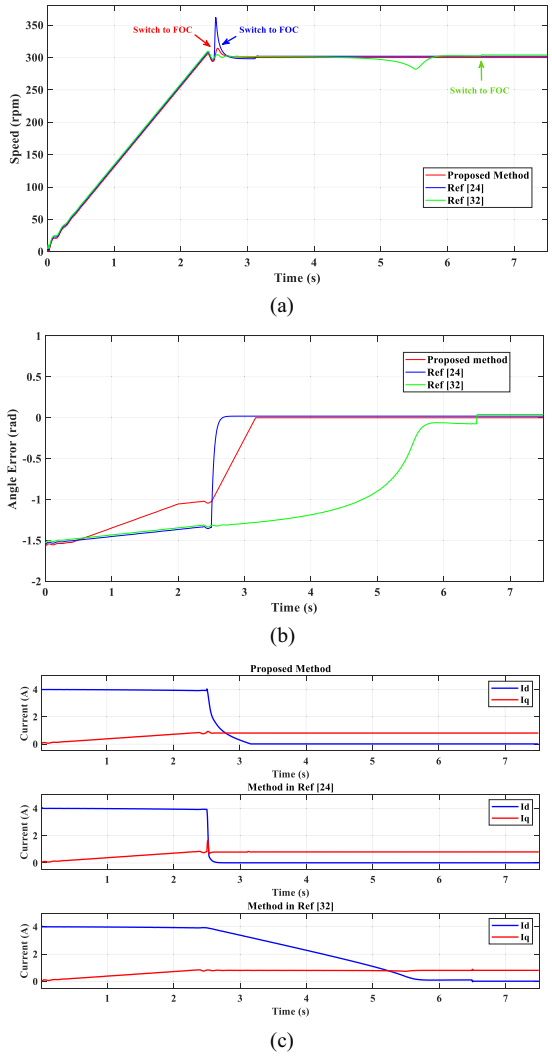

Fig. 16. Performance comparison of the proposed method versus conventional methods. (a) Speed response. (b) Angle error between virtual synchronous d^*q^*-reference frame and actual rotor dq frame. (c) Real dq-axis currents.

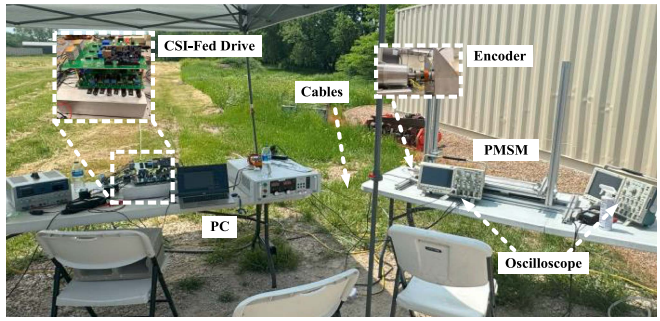

Fig. 17. Experimental setup of the CSI-fed PMSM drive system with a long cable connection for submersible pump.

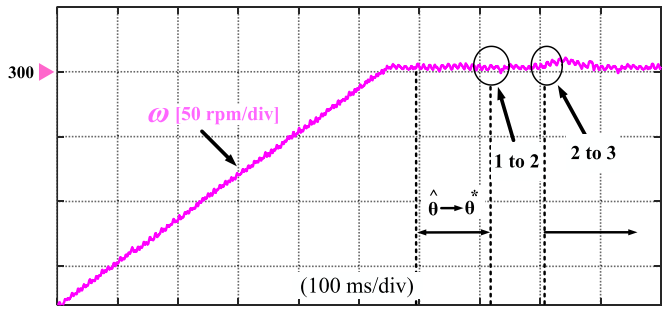

Fig. 18. Experimental results of the motor speed during different stages of the proposed startup strategy.

Fig. 18 presents the experimental results of the motor speed throughout all stages of the transition from the I-f method to sensorless FOC, when the proposed smooth transition strategy is applied. As in the simulation tests, the motor accelerates to 300 r/min, where the estimated speed is accurately captured. The estimated position is then aligned with the virtual reference frame using the compensator. Subsequently, the terminal transitions from 1 to 2 without any speed or current oscillation. Finally, the terminal shifts from 2 to 3, and the position error between the estimated and actual position is compensated using

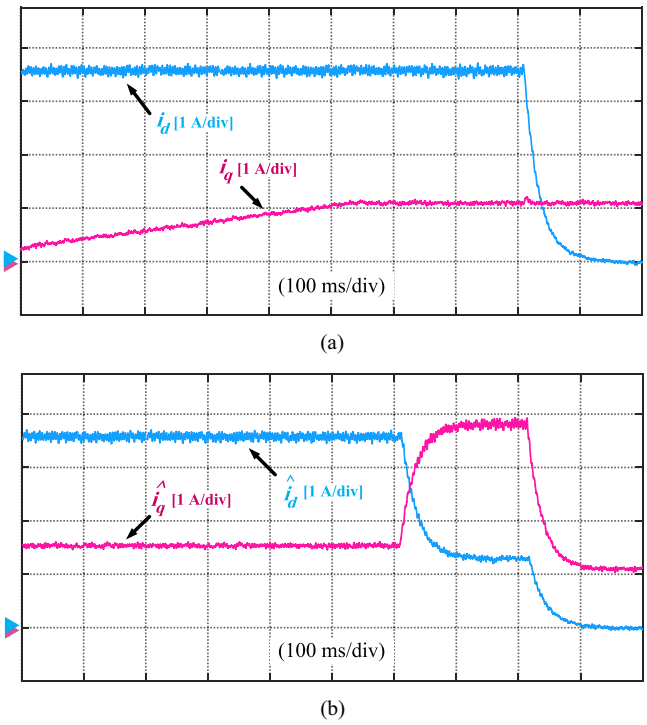

Fig. 19. Experimental results of the proposed startup strategy throughout all stages of the transition from the I-f method to sensorless FOC. (a) Real dq-axis currents. (b) Estimated $\hat{d}\hat{q}$-axis currents.

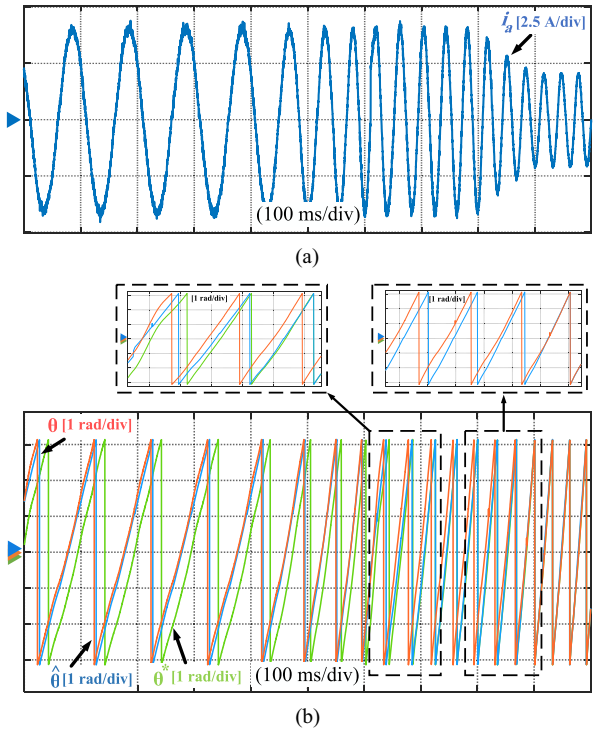

Fig. 20. Experimental results of the proposed startup strategy throughout all stages of the transition from the I-f method to sensorless FOC. (a) Phase A current. (b) Virtual synchronous, real, and estimated positions.

the proposed strategy. The experimental results demonstrate the effectiveness of the proposed startup strategy, exhibiting minimal speed oscillation.

Fig. 19 illustrates the experimental results of the real dq-axis and estimated $\hat{d}\hat{q}$-axis currents during different stages of the proposed startup strategy. As is shown in Fig. 19(a), during the speed ramp-up, the real q-axis current increases with respect to the speed until 300 r/min. The real d-axis current will also drop to zero once the terminal switches from 2 to 3, as the proposed rotor error compensation strategy is employed. The results indicate a minimal overshoot in the real q-axis current, demonstrating the effectiveness of the proposed smooth transition to sensorless control strategy. Fig. 19(b) illustrates the estimated $\hat{d}\hat{q}$-axis currents during startup. As shown, once the terminal switches from 2 to 3 and the proposed rotor error compensation strategy is applied, the error between the real and estimated frames is quickly eliminated, leading to the estimated $\hat{d}\hat{q}$-axis currents aligning with the real dq-axis currents.

Fig. 20(a) presents the experimental results of phase A current during all stages of the proposed startup. As shown, the current amplitude decreases when the proposed rotor error compensation method is applied, and the error between the estimated and real frames is eliminated. Fig. 20(b) presents the experimental results of the virtual synchronous, estimated, and real positions throughout all stages of the transition from the I-f method to sensorless FOC, with two zoomed-in views highlighting the transitions when the terminal switches from 1 to 2 and from 2 to 3. Initially, the I-f method is employed to start the motor from standstill, gradually accelerating to a stable target speed where the back EMF becomes high enough to estimate the position using the PLL and observer, with both switches connected to terminal 1. Next, the compensator shown in Fig. 3 reduces the error between the estimated and reference positions to zero, preparing the system for the switch to terminal 2. Finally, the switches are moved to terminal 3, where the PLL output initially shows the same error calculated by the compensator; however, this position error is corrected using the proposed error compensation strategy, as described in (30) and (31).

Fig. 21 presents the experimental results of angle errors between different rotating frames throughout all stages of the proposed startup strategy. As is shown in Fig. 21(a), the Angle error between actual rotor dq frame and estimated $\hat{d}\hat{q}$ frame will be eliminated after the terminal is switched from terminal 2 to 3, as the proposed error compensation strategy is applied. This shows the effectiveness of the error compensation strategy. The estimated $\hat{d}\hat{q}$ frame will be aligned with virtual synchronous d^*q^*-reference frame using the compensator before switching from terminal 1 to 3, as is shown in Fig. 21(b).

The proposed rotor position error compensation method effectively eliminates misalignment between the estimated and actual rotor positions, improving d-axis current control and reducing copper losses, leading to enhanced efficiency. Rotor position errors, even small ones, can cause torque ripple, increased losses, and degraded performance in PMSM drives. The compensation strategy ensures accurate alignment of the reference frame with

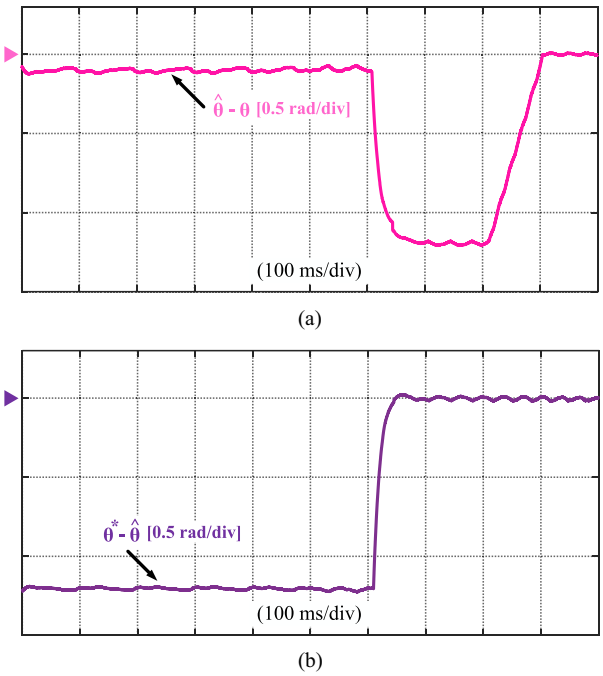

Fig. 21. Experimental results of the proposed startup strategy throughout all stages of the transition from the I-f method to sensorless FOC. (a) Angle error between actual rotor dq frame and estimated $\hat{d}\hat{q}$ frame. (b) Angle error between estimated $\hat{d}\hat{q}$ frame and virtual synchronous d^*q^*-reference frame.

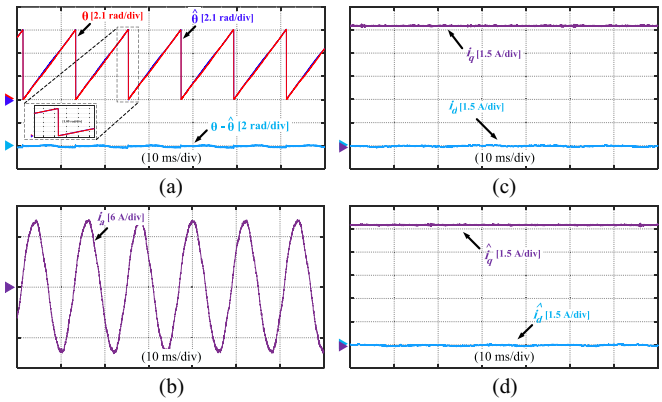

Fig. 22. Experimental steady-state performance at the speed of 850 rpm with rotor error position compensation. (a) Real and estimated positions. (b) Phase a current. (c) Actual rotor dq-axis currents. (d) Estimated rotor $\hat{d}\hat{q}$-axis currents.

the rotor position before transitioning to sensorless FOC, minimizing d-axis current errors and maintaining the desired q-axis current for efficient torque generation. As shown in Figs. 22 and 23 at 850 r/min, the real d-axis current decreases from 1.8 A to zero, while the estimated q-axis current reduces slightly by 3.6% from 8.05 to 7.76 A. Additionally, the phase current slightly drops, confirming that the error compensation reduces unnecessary power dissipation. The method also reduces the estimation error by 0.16 rad, demonstrating the effectiveness of the compensation strategy in improving position accuracy and system performance, ensuring stable and efficient operation during startup.

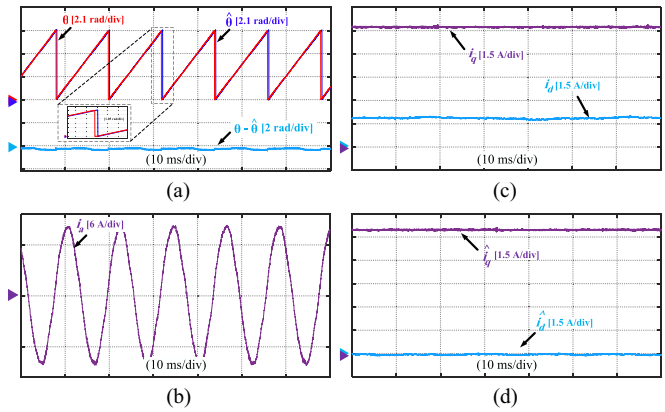

Fig. 23. Experimental steady-state performance at the speed of 850 r/min without rotor error position compensation. (a) Real and estimated positions. (b) Phase a current. (c) Actual rotor dq-axis currents. (d) Estimated rotor $\hat{d}\hat{q}$-axis currents.

VI. Conclusion

This article presents a novel startup strategy that ensures a smooth transition to sensorless FOC for CSI-fed PMSM drives, specifically tailored for submersible pump applications. The proposed method overcomes the challenges of accurately calculating the minimum q-axis current and real-estimated frame alignment errors, offering a more practical and reliable approach. By leveraging an error compensation strategy, the transition from the I-f startup method to sensorless FOC is seamlessly achieved, with the error between the estimated and real rotor positions progressively corrected. This results in minimal speed and current oscillations, thereby enhancing both the performance and stability of the drive system. This method offers a robust, adaptive shift from I-f startup to FOC under varying conditions. Additionally, the proposed compensation method corrects rotor discrepancies from dead-time, control delays, and parameter variations, improving torque and flux control, reducing d-axis current and torque ripple, lowering copper losses, and eliminating steady-state errors. This results in a faster, more reliable transition, avoiding prolonged startup durations and enhancing system stability. Simulation and experimental results confirm the effectiveness of the proposed strategy, demonstrating its ability to reduce torque fluctuations and to improve the overall efficiency of the system during critical transition stages. The work presented here represents a significant contribution to the field of sensorless control for CSI-fed PMSM drives, providing a robust solution for industrial applications that demand high reliability and smooth operation.

References

[1] D. Jin and L. Liu, "Adaptive second-order disturbance observer-based position sensorless drive strategy for PMSM," *IEEE Trans. Power Electron.*, vol. 39, no. 12, pp. 16415–16428, Dec. 2024.

[2] G. Bi et al., "High-frequency injection angle self-adjustment based online position error suppression method for sensorless PMSM drives," *IEEE Trans. Power Electron.*, vol. 38, no. 2, pp. 1412–1417, Feb. 2023.

[3] W. Xu, S. Qu, L. Zhao, and H. Zhang, "An improved adaptive sliding mode observer for middle- and high-speed rotor tracking," *IEEE Trans. Power Electron.*, vol. 36, no. 1, pp. 1043–1053, Jan. 2021.

[4] D. D. Patel, I. Boldea, B. Fahimi, and M. B. Fard, "High torque density double stator PM synchronous machine," in *Proc. IEEE Transp. Electrific. Conf. Expo*, 2024, pp. 1–6.

[5] Y. Zuo, C. Lai, and K. L. V. Iyer, "A review of sliding mode observer based sensorless control methods for PMSM drive," *IEEE Trans. Power Electron.*, vol. 38, no. 9, pp. 11352–11367, Sep. 2023.

[6] M. Bahrami-Fard, B. M. Mosammam, M. H. Ghaderi, D. D. Patel, P. Balsara, and B. Fahimi, "An effective cooling system for high torque electric motors using microchannels and two-phase coolants," in *Proc. IEEE Transp. Electrific. Conf. Expo*, 2024, pp. 1–6.

[7] G. Wang, M. Valla, and J. Solsona, "Position sensorless permanent magnet synchronous machine drives—A review," *IEEE Trans. Ind. Electron.*, vol. 67, no. 7, pp. 5830–5842, Jul. 2020.

[8] G. Bi et al., "High-frequency injection angle self-adjustment based online position error suppression method for sensorless PMSM drives," *IEEE Trans. Power Electron.*, vol. 38, no. 2, pp. 1412–1417, Feb. 2023.

[9] Y.-R. Lee and S.-K. Sul, "Switching frequency signal-injection sensorless control in dual three-phase PMSM robust to nonideal characteristics of inverter system," *IEEE Trans. Power Electron.*, vol. 39, no. 7, pp. 8540–8552, Jul. 2024.

[10] G. Wang, D. Xiao, G. Zhang, C. Li, X. Zhang, and D. Xu, "Sensorless control scheme of IPMSMs using HF orthogonal square-wave voltage injection into a stationary reference frame," *IEEE Trans. Power Electron.*, vol. 34, no. 3, pp. 2573–2584, Mar. 2019.

[11] G. Wang, L. Yang, G. Zhang, X. Zhang, and D. Xu, "Comparative investigation of pseudorandom high-frequency signal injection schemes for sensorless IPMSM drives," *IEEE Trans. Power Electron.*, vol. 32, no. 3, pp. 2123–2132, Mar. 2017.

[12] A. Benevieri, A. Formentini, M. Marchesoni, M. Passalacqua, and L. Vaccaro, "Sensorless control with switching frequency square wave voltage injection for SPMSM with low rotor magnetic anisotropy," *IEEE Trans. Power Electron.*, vol. 38, no. 8, pp. 10060–10072, Aug. 2023.

[13] A. Andersson and T. Thiringer, "Motion sensorless IPMSM control using linear moving horizon estimation with Luenberger observer state feedback," *IEEE Trans. Transp. Electrific.*, vol. 4, no. 2, pp. 464–473, Jun. 2018.

[14] M. Bahrami-Fard, M. G. Korrani, M. Rastegar, P. Balsara, and B. Fahimi, "Error compensation strategy in encoderless surface mounted PMSM drives," in *Proc. IEEE Energy Convers. Congr. Expo.*, 2024, pp. 6104–6109.

[15] F. G. Z. Yin, Y. Zhang, C. Du, G. Li, and X. Sun, "A review of nonlinear Kalman filter applying to sensorless control for AC motor drives," *CES Trans. Elect. Mach. Syst.*, vol. 3, no. 4, pp. 351–362, Dec. 2019.

[16] L. Zhang, Z. Chen, X. Yu, J. Yang, and S. Li, "Sliding-mode-based robust output regulation and its application in PMSM servo systems," *IEEE Trans. Ind. Electron.*, vol. 70, no. 2, pp. 1852–1860, Feb. 2023.

[17] M. Bahrami-Fard, M. G. Korrani, M. Rastegar, P. Balsara, and B. Fahimi, "Adaptive PLL-based sensorless control for CSI-fed PMSM drives used in submersible pumps," in *Proc. IECON- 50th Annu. Conf. IEEE Ind. Electron. Soc.*, 2024, pp. 1–6.

[18] M. Seilmeier and B. Piepenbreier, "Sensorless control of PMSM for the whole speed range using two-degree-of-freedom current control and HF test current injection for low-speed range," *IEEE Trans. Power Electron.*, vol. 30, no. 8, pp. 4394–4403, Aug. 2015.

[19] L. Ding, Y. W. Li, N. R. Zargari, and R. Paes, "Sensorless control of CSC-fed PMSM drives with low switching frequency for electrical submersible pump application," *IEEE Trans. Ind. Appl.*, vol. 56, no. 4, pp. 3799–3808, Jul./Aug. 2020.

[20] S. Yang, Z. Yin, C. Tong, Y. Sui, and P. Zheng, "Active damping current control for current-source inverter-based PMSM drives," *IEEE Trans. Ind. Electron.*, vol. 70, no. 4, pp. 3549–3560, Apr. 2023.

[21] Z. Wang, Y. Xu, P. Liu, Y. Zhang, and J. He, "Zero-voltage-switching current source inverter Fed PMSM drives with reduced EMI," *IEEE Trans. Power Electron.*, vol. 36, no. 1, pp. 761–771, Jan. 2021.

[22] L. Ding, Y. W. Li, and N. R. Zargari, "Discrete-time SMO sensorless control of current source converter-fed PMSM drives with low switching frequency," *IEEE Trans. Ind. Electron.*, vol. 68, no. 3, pp. 2120–2129, Mar. 2021.

[23] Y. Xu, C. Lin, J. Xing, Q. Zeng, and J. Sun, "I-f starting rapid and smooth transition method of full-speed sensorless control for low current harmonic ultra-high-speed PMSM," in *Proc. IEEE Appl. Power Electron. Conf. Expo.*, 2022, pp. 1820–1826.

[24] M. Fatu, R. Teodorescu, I. Boldea, and G. D. Andreescu, "I-f starting method with smooth transition to EMF based motion-sensorless vector control of PM synchronous motor/generator," in *Proc. Conf. Rec. Power Electron. Spec. Conf.*, 2008, pp. 1481–1487.

[25] S. V. Nair, K. Hatua, N. D. Prasad, and D. K. Reddy, "A quick I-f starting of PMSM drive with pole slipping prevention and reduced speed oscillations," *IEEE Trans. Ind. Electron.*, vol. 68, no. 8, pp. 6650–6661, Aug. 2021.

[26] X. Song, J. Fang, B. Han, and S. Zheng, "Adaptive compensation method for high-speed surface PMSM sensorless drives of EMF-based position estimation error," *IEEE Trans. Power Electron.*, vol. 31, no. 2, pp. 1438–1449, Feb. 2016.

[27] G. Wang, T. Li, G. Zhang, X. Gui, and D. Xu, "Position estimation error reduction using recursive-least-square adaptive filter formodel-based sensorless interior permanent-magnet synchronous motor drives," *IEEE Trans. Ind. Electron.*, vol. 61, no. 9, pp. 5115–5125, Sep. 2014.

[28] G. Zhang, G. Wang, D. Xu, and N. Zhao, "ADALINE-network-based PLL for position sensorless interior permanent magnet synchronous motor drives," *IEEE Trans. Power Electron.*, vol. 31, no. 2, pp. 1450–1460, Feb. 2016.

[29] T. Mannen and H. Fujita, "Dead-time compensation method based on current ripple estimation," *IEEE Trans. Power Electron.*, vol. 30, no. 7, pp. 4016–4024, Jul. 2015.

[30] S. Jung, H. Kobayashi, S. Doki, and S. Okuma, "An improvement of sensorless control performance by a mathematical modelling method of spatial harmonics for a SynRM," in *Proc. Power Electron. Conf.*, 2010, pp. 2010–2015.

[31] Y. Park and S.-K. Sul, "Implementation schemes to compensate for inverter nonlinearity based on trapezoidal voltage," *IEEE Trans. Ind. Appl.*, vol. 50, no. 2, pp. 1066–1073, Mar./Apr. 2014.

[32] Z. Wang, K. Lu, and F. Blaabjerg, "A simple startup strategy based on current regulation for back-EMF-based sensorless control of PMSM," *IEEE Trans. Power Electron.*, vol. 27, no. 8, pp. 3817–3825, Aug. 2012.

[33] J. Xing, Z. Qin, C. Lin, and X. Jiang, "Research on startup process for sensorless control of PMSMs based on I-f method combined with an adaptive compensator," *IEEE Access*, vol. 8, pp. 70812–70821, 2020.

[34] M.-S. Rho and S.-Y. Kim, "Development of robust starting system using sensorless vector drive for a microturbine," *IEEE Trans. Ind. Electron.*, vol. 57, no. 3, pp. 1063–1073, Mar. 2010.

[35] A. Stirban, I. Boldea, G.-D. Andreescu, D. Iles, and F. Blaabjerg, "Motion sensorless control of BLDC PM motor with offline FEM info assisted state observer," in *Proc. 12th Int. Conf. OPTIM*, 2010, pp. 321–328.

[36] S. Jung, H. Kobayashi, S. Doki, and S. Okuma, "An improvement of sensorless control performance by a mathematical modelling method of spatial harmonics for a SynRM," in *Proc. Power Electron. Conf.*, 2010, pp. 2010–2015.

[37] Y. Park and S.-K. Sul, "Implementation schemes to compensate for inverter nonlinearity based on trapezoidal voltage," *IEEE Trans. Ind. Appl.*, vol. 50, no. 2, pp. 1066–1073, Mar./Apr. 2014.